SEISMOLOGICAL STUDIES
IN THE CHINSHAN FAULT AREA

KUANG-JUNG CHEN[1], YIH-HSIUNG YEH[2], HORNG-YUAN YEN[2] and CHENG-HORNG LIN[2]

1. Institute of Earth Sciences, National Taiwan Normal University, Taipei, Taiwan, R.O.C.
2. Institute of Earth Sciences, Academia Sinica, Taipei, Taiwan, R.O.C.

ABSTRACT

A temporary seismographic network with twelve three-component digital stations was deployed in the Chinshan-Tanshui area, northern Taiwan in 1989/1990. Data recorded by this network together with those by three stations of the Taiwan Telemetered Seismographic Network (TTSN) were analyzed to determine the characteristics of the Chinshan fault. Both the distributions of the P-wave travel time residuals and t_p^* values indicate that the Chinshan fault might exist at the location that is inferred by surface geologic data. This fault reveals low seismicity. The focal depth profile shows the dip of the fault is about $55°$ to the southeast. The activity of the Chinshan fault may be normal or thrust, depending on the stress pattern in this area.

Key words: P-wave travel time, t_p^* values

INTRODUCTION

Microearthquakes in general occur in large numbers and often have distinct spatial distribution. Seismicity data can be collected in short time intervals to delineate the pattern of recent tectonic activity. Thus, through a microearthquake survey, one can obtain significant seismologic and tectonic insight in this study area. The main purpose of the present microearthquake observation are : (1) to understand the current seismicity (2) to ascertain whether there are active faults, and (3) to determine the characteristics of the active faults if they exists.

Chen and Yeh (1991) studied the Chinshan fault by using the gravity and microearthquake data. In their study, however, only the earthquake data obtained from vertical-component analogical seismograms were used. For a more detailed survey, a temporary seismographic network with twelve three-component digital seismographs in the same area as that of Chen and Yeh (1991) was deployed in 1989/1990. To augment the data set, seismograms from three stations of the Taiwan Telemetered Seismographic Network (TTSN) were also used. The purpose of this study is to provide a better understanding of the seismological characteristics of the Chinshan fault and its vicinity.

In this paper, four different analyses were performed. First, the P-wave travel time residuals at seismographic stations were calculated in an attempt to locate the Chinshan fault. A Similar application had been previously made to locate a magma chamber (Achauer *et al.*, 1986). Second, the t_p* values determined from spectral decay were used to study the anelastic properties of the crust (e.g., Reiter and Monfort, 1977). Third, the seismicity pattern was used as a mean to locate the Chinshan fault. Finally, the focal mechanisms   solutions were determined to infer the mechanic behavior of the Chinshan fault.
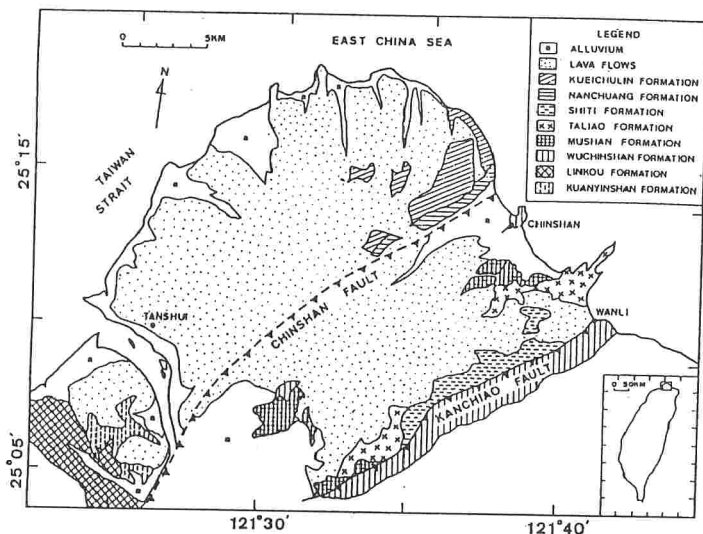

Figure 1. Simplified geologic map of the study area (After Chen and Yeh (1991)).

GEOLOGIC SETTINGS

Early and late Miocene sedimentary rocks and Pleistocene volcanic rocks are exposed in the study area. The early Miocene rocks are the Wuchihshan Formation, the Mushan Formation and the Talio Formation. The late Miocene rocks are the Nanchuang Formation and the Kueichulin Formation. The Pleistocene rocks are the Kuanyinshan Formation, Linkou Formation and volcanic breccias. As given by Chang (1986), Chou (1962), Hsu (1967) and Hsu (1981), the surface geologic data in the study area are shown in Figure 1, and the characteristics of the above formations can be summarized as follows:

1. Wuchishan Formation:
   The maximum thickness of this formation is estimated at more than 1200 meters. Massive white sandstone is predominant in this formation and belongs to the category of orthoquartzite or psotoquartzite.

2. Mushan Formation:
   This formation is characterized by white, medium- to coarse-grained quartzose sandstones

which are mostly psotoquartzite in composition. Only the upper part of this formation with a thickness of 300 meters is exposed in the study area.

3. Taliao Formation:

The thickness of this formation is about 500-550 meters. This formation is a marine unit directly overlying the coal-bearing Mushan Formation. The type locality of this formation bears a monotonous sequence of thick-bedded to massive sandstone alternated with thin and thick beds of shale and silty shale.

4. Nankang Formation:

The total thickness of this formation is about 700-750 meters in the study area. It is composed of thick- to thin-bedded, light bluish gray, fine-grained calcareous sandstone and dark gray shale or siltstone.

5. Nanchuang Formation:

The total thickness of this formation is 500 to 600 meters. This formation is distributed in the southeastern part of the study area. It is composed largely of white sandstone.

6. Kueichulin Formation:

This formation is generally divided into two units, the Tapu Formation below and the Erhchiu Formation above. The Tapu Formation is composed of thick-bedded, light gray muddy sandstone and has a thickness of 300-400 meters. The Erhchiu Formation in the upper part is also composed of thick-bedded, light bluish gray muddy sandstone and usually has a thickness of 400 to 500 meters.

7. Linkou Formation:

This formation comprises all the gravels and the lateritic mantle. The gravel is composed mainly of lithic and quartzite sandstones. The total thickness of this formation is about 200 meters.

8. volcanic rocks:

The volcanic rocks in this area consist of volcanic breccias, andesitic lava flows and andesite detritus. The tuffaceous breccia is widely distributed in the northwestern part of the study area and forms a gently west-dipping platform with a long cliff on the coast. This platform ranges from 50 to 260 meters in elevation. The thickness of the tuffaceous breccia is estimated at nearly 120 meters. The andesite detritus consists of volcanic ash and weathered andesite blocks which are scattered on the hill slopes.

The known structural features of the study area are the Wanli homocline, the Chinshan fault, the Tiaoshih syncline and the Kanchiao thrust fault (Hsu, 1967). The Wanli homocline extends from the northwest of the Kanchiao fault to the Huangchi stream and is bounded on the northwest by the Chinshan fault. The Chinshan fault, also termed the Hsinchuang fault, is completely concealed under alluvium in the Chinshan Valley. The trace of the Chinshan fault as shown in Figure 1 is inferred from the gravity data by Hsu (1967). This fault strikes $N\,56°\,E$ and approximately follows the northwestern edge of the Chinshan Valley, extending inland from the coast near Chungchiao to Huangchitou and then into the Tatun volcano area. The Chinshan fault is inferred to be a thrust fault dipping to the southeast, the hanging wall being composed of the base of the Wuchihshan Formation and the footwall of the lower part of the Nanchuang Formation. The fault separates the Wanli homocline in the upper block from the Tiaoshih syncline in the lower block. The Tiaoshih syncline is limited on the southeast by the Chinshan fault, and its axial trace trends $S\,56°\,W$. The middle part of this syncline is covered entirely by volcanic breccias and lava flows from the Tatun Volcano Group. The Kanchiao thrust fault strikes $N\,60°\,E$ and approximately follows the Masuchi stream from the Kanchiao to

Table 1. Parameters of seismographic stations.

STATION RECORDER	CODE	LATITUDE (°) (')	LONGITUDE (°) (')	ELEVATION (m)	
Kanchiao	CKC	25 09.73	121 37.63	260	SSR-1
Laumei	CLM	25 15.28	121 32.91	140	SSR-1
Pintin	CPT	25 13.53	121 32.38	520	SSR-1
Sueiwei	CSW	25 10.70	121 31.80	690	SSR-1
Suanshih	CSS	25 07.50	121 34.10	240	SSR-1
Chinshan	CKS	25 13.19	121 36.87	13	SSR-1
Tienmu	CTM	25 07.90	121 31.10	95	SSR-1
Tanshui	CTS	25 10.97	121 28.20	158	SSR-1
Chugaulin	CCK	25 08.79	121 33.79	500	SSR-1
Shihdi	CCT	25 09.09	121 36.54	265	SSR-1
Sanho	CSH	25 13.49	121 35.05	115	SSR-1
Pesinchung	CHC	25 11.90	121 30.41	440	SSR-1
Wus Temp.	KWS	25 09.43	121 29.73	320	SSR-1
Huangshan	KHS	25 11.87	121 35.57	345	SSR-1
Neiliaw	KNL	25 09.49	121 41.14	70	SSR-1
Kuangpeiden	KKP	25 05.79	121 38.03	95	SSR-1
Tuku	KTK	25 01.36	121 37.35	283	SSR-1
Tungshan	KTS	25 03.22	121 41.73	153	SSR-1
Tungchiken	KTC	25 05.12	121 44.35	90	SSR-1
Koushen	TWX	25 11.93	121 39.70	40	(TTSN)
Chanhwa	TWY	25 16.55	121 35.98	20	(TTSN)
Neihu	TWZ	25 05.82	121 34.74	280	(TTSN)
Chihnankung	TWA	24 58.82	121 35.02	260	(TTSN)
Wulai	TWU	24 52.65	121 32.02	330	(TTSN)
Kuanyinshan	TWS1	25 06.05	121 25.06	60	(TTSN)

Figure 2. Locations of temporary seismographic stations (denoted by hollow triangles) and the TTSN stations (denoted by solid squares)
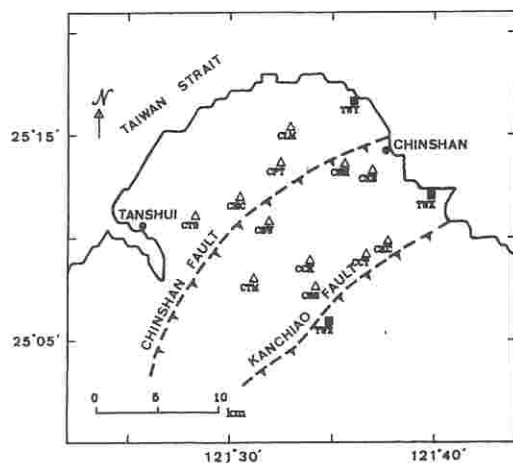
Wanli and into the sea. The fault plane follows the lower part of the Wuchishan Formation, separating the Wanli homocline in the lower block from the Tawulun homocline in the upper block. The fault plane near the surface dips from 45° to 50° southeastward.

TEMPORARY SEISMOGRAPHIC NETWORK

The basic data set for this study is composed mostly of seismograms from a temporary seismographic network and partly of those from the TTSN. The temporary seismographic network, consisting of twelve stations and covering an area of about 200 km², was deployed in the Chinshan-Tanshui area from November 23, 1989 to April 10, 1990. The station parameters are listed in Table 1, and the geographic locations are shown in Figure 2. At each temporary station, a 16-bit SSR-1 was used as the recorder. In this study, the sample rate was set at 200 samples/per second. The STA/ LTA ratio trigger was used in this experiment. The SSR-1 uses a 16-bit A to D converter to provide a 96 dB dynamic range. Each station is equipped with a three-component sensor, with a natural frequency of 4 Hz. Figure 3 illustrates the system response curves (velocity type) of the temporary network and the TTSN.
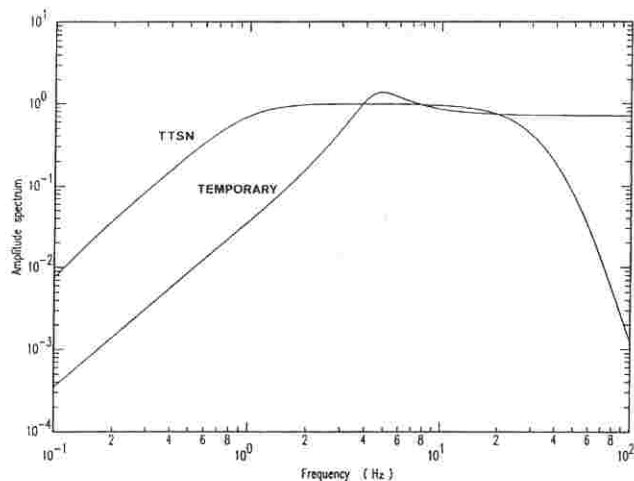

Figure 3. System response curves of the SSR-1 and the sensor of a typical TTSN station.

Events recorded simultaneously by more than four stations were analyzed. Earthquake locations were determined by using both P- and S- waves. HYPO71 (Lee and Lahr, 1972) was used to determine the hypocentral location and origin time of the earthquake. The horizontally layered crust model used was as follows:

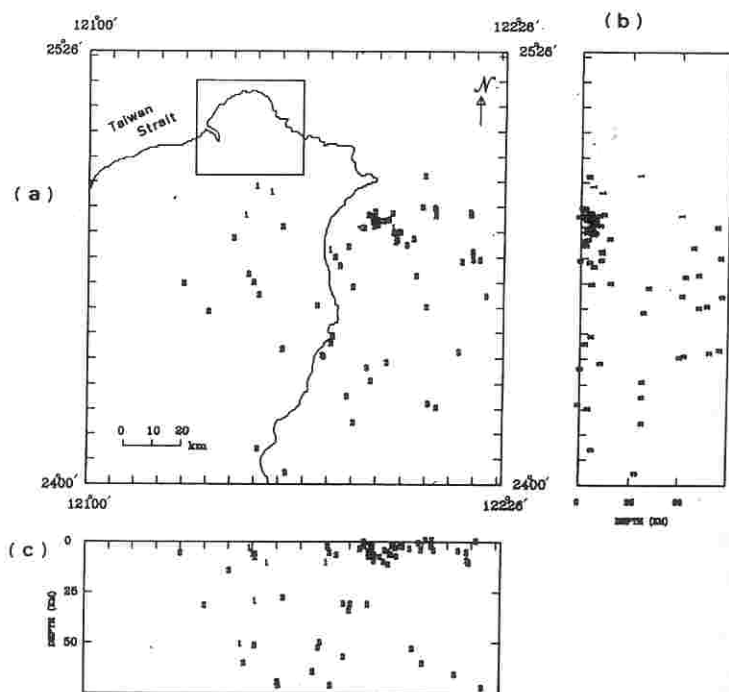| Layer	Depth (km)	P-velocity (km/sec)	S-velocity (km/sec)
1	0 - 9	5.84	3.28
2	9 - 17	6.07	3.41
3	17 - 36	6.73	3.78
4	> 36	7.79	4.38

Figure 4. (a) Epicenters used to calculate the P-wave travel time residual; (b) depth distribution of events along the NS direction; (c) depth distribution of events along the EW direction. The numbers represent the magnitude of events.

This model was derived by Yeh and Tsai (1981). The correction for elevation due to travel time was made by the following formula:

$$dt = - H / V \qquad (1)$$

where dt represents the elevation correction of travel time, **H** is the station elevation in meters, and **V** is the average P-wave velocity of rocks above sea level in m/sec. (1800 m/sec was assumed in this area)

The earthquake magnitude M_D was determined from the signal duration by using the formula (Lee *et al.*, 1972):

$$M_D = - 0.87 + 2.0 \log T + 0.0035 D \qquad (2)$$

where **T** represents the total signal duration in seconds, and **D** represents the epicentral distance in kilometers.

Table 2. Statistics of the P-wave residual (unit: second)

Station	KKP	TWX	TWY	TWZ	TWA	TWU	TWR	TWB1	TWS1	KSH	KWS	KNL	KTK	KTC
Mean	0.06	0.05	0.22	0.02	0.07	-0.20	0.03	-0.15	0.20	0.22	0.06	0.10	0.06	0.03
Std Err	0.02	0.03	0.03	0.02	0.02	0.02	0.02	0.03	0.03	0.04	0.03	0.03	0.02	0.02
95% Conf	0.04	0.06	0.06	0.04	0.04	0.05	0.05	0.06	0.06	0.09	0.07	0.08	0.05	0.06

Figure 5. Distribution of the P-wave travel time residual (the dashed lines show the probable exposed traces of the Chinshan fault and the Kanchiao fault; the contour lines with hatches denote the depression, and the hatches point toward the depression).
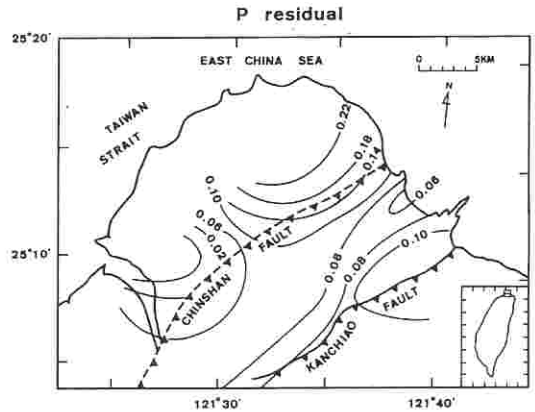
P-WAVE TRAVEL TIME RESIDUALS

The P-wave travel time residual at the ith station for the jth event is defined by:

$$R_{ij} = T^o_{ij} - T^t_{ij} \qquad (3)$$

where T^o_{ij} is the observed P-wave arrival time at the ith station for the jth event, and Ttij is the theoretical travel time based on the located hypocenter. Station KKP was selected as a "standard station" in this study, since it (the site) has lower background noise than the others. If R_{ij} denotes the absolute time residual observed at station KKP for the jth event, then the relative time residual at the ith station for the same event is defined as:

$$r_{ij} = R_{ij} - R_{kj} \qquad (4)$$

Any uncertainty of the calculated travel time is caused by those errors in the hypocenter or origin time. Since any such error affects the travel time residuals R_{ij} and R_{kj}, the error in r_{ij} is minimized. Any variation in r_{ij}, therefore, may be attributed to local structural changes with respect to the kth station.

Ninety-five events (Figure 4) were used for calculating the P-wave travel time residuals.

These events were selected for as wide a range of distance, azimuth and depth as possible so as to have a uniform distribution of rays. Table 2 shows the relative residual and its standard deviation for each station. Figure 5 shows the surface plot of relative residuals over the study area. Two hogback shapes can be delineated. The lines of summit of these two shapes mostly coincide with the strike of the Chinshan fault and the Kanchiao fault respectively. These two faults were previously recognized from geologic data (Ho, 1974). The values of the delay in the Chinshan fault area were larger than those in the Kanchiao fault area. In general, a positive larger P-wave residual indicates a bigger delay during (the) propagation. This effect may be caused by many factors, such as a low velocity zone, rupture zone or fault zone. In the present study, the high area of P-wave residuals is considered to have mainly been caused by the rupture of the Chinshan fault.

t_p^* VALUES

Seismic wave attenuation has long been regarded as the key indicator of the Earth's anelastic properties. Numerous measurements have been made using spectral methods for body waves, surface waves and free oscillations (e.g., Bakun et al., 1976; Bakun & Bufe, 1975; Barker & Stevens, 1983; Ben-Menahem et al., 1972).

Q^{-1} is a dimensionless quantity that indicates the energy dissipation per radian of the seismic waves due to the anelasticity of the material. Laboratory studies showed the independence of Q^{-1} on frequency (Knopoff, 1964). In fact, the theoretical Q^{-1} values vary significantly with frequency for materials of uniform composition and grain size. However, in a composite viscoelastic material with a range of relaxation time, Q^{-1} varies smoothly with frequency and may even be considered a constant over a narrow frequency band (Kanamori & Anderson, 1977). This consideration was applied to study the seismic wave attenuation by using the reduced spectral ratio technique (Teng, 1968; Solomon, 1972, 1973).

The effect of Q^{-1} on seismic waves along the ray path from the source can be estimated by multiplying the source spectrum, $S(f)$, by an exponential factor of $e^{-\pi f t^*}$, i.e.,

$$A(r, f) = A_o (r, f) \; e^{-\pi f t^*} \tag{5}$$

where

$$t^* = \int \frac{dr}{QV} \tag{6}$$

In Equation (6), V is the wave velocity, Q is the spatial attenuation factor, and the integral is along the ray path (Kanamori, 1967).

Based on Gladwin & Stacey (1974), the empirical relationship between the rise time of a pulse, t and its propagation time, t is:

$$t = t_o + \int c \frac{dt}{Q} \tag{7}$$

Where c is a constant of 0.5, and t_o is the initial rise time at t = 0. The rise time has been

used to measure variations in the anelastic properties of the seismic exploration data. For example, Reiter and Monfort (1977) successfully located the San Andreas and Calaveras faults in central California by the rise time data. The rise time can be accurately determined from seismic exploration records but not so easily from a seismogram of a natural earthquake. According to the definition of t* (Equation (6)), Equation (7) can be rewritten as:

$$t = t_o + c\, t^*$$ (8)

This equation shows that t* is proportional to the rise time. In the present study, t* was applied instead of the rise time to deduce the anelastic properties since the seismograms of natural earthquakes were used.

The spectrum of displacement, observed at a site in distance r from the epicenter, $A(r, f)$ may be approximated by:

$$A(r,f) = (2\pi f)^2 S(f) G(r,f) e^{-\pi f t^*}$$ (9)

where G (r,f) represents the geometrical spreading, and S (f) is the displacement spectrum of radiation at the source. In a certain frequency range (e.g., 1-40 Hz), the Brune source theory (Brune,1970) states that the source displacement spectrum varies with ω^{-2} beyond the corner frequency and is flat in the range among zero (frequency) and corner frequency. Using this assumption, $A_o(r,f)$ in (5) is frequency independent; thus, after the natural logarithm of both sides is taken. Equation (5) can be rewritten as:

$$\ln A\,(r,f) = \ln A_o(r) - \pi f\, t^*$$ (10)

where $A_o(r)$ also includes the geometric spreading term which is independent of frequency. Since the geometric spreading term is also frequency-independent, the value of $A_o(r)$ only affects the level of the spectrum and causes no effect on t^*. The differentiation of Equation (10) with respect to f leads to:

$$\frac{d(\ln A(r,f))}{df} = -\pi t^*$$ (11)

Equation (11) defines the slope of the straight line described by Equation (10). Thus, the slope $-\pi t^*$ can be determined by fitting the observed data points of the spectrum with a straight line using the least-squares method in a certain frequency range. Therefore, the t* value can be calculated by dividing the slope by $-\pi$. Due to the limited dimensions of the area of interest (Figure 2) and the type of data available, it was required that the t* values be determined in the high frequency band (f > 4Hz). Many techniques have been developed to study high-frequency attenuation at near and regional distances. At high frequencies, the most widely employed source spectrum model is the ω^2 model which assumes that S(f) is proportional to f^2 (Brune, 1970). The present authors have used the Fourier spectrum over frequencies between the eigen-frequency of the seismometer (about 1 Hz or 4Hz) and 24 Hz because the spectrum for frequencies lower than the eigen-frequency may be rather unreliable, and because that for frequencies higher than 24 Hz has a very small amplitude due to a high cut-off filter in the recording system.
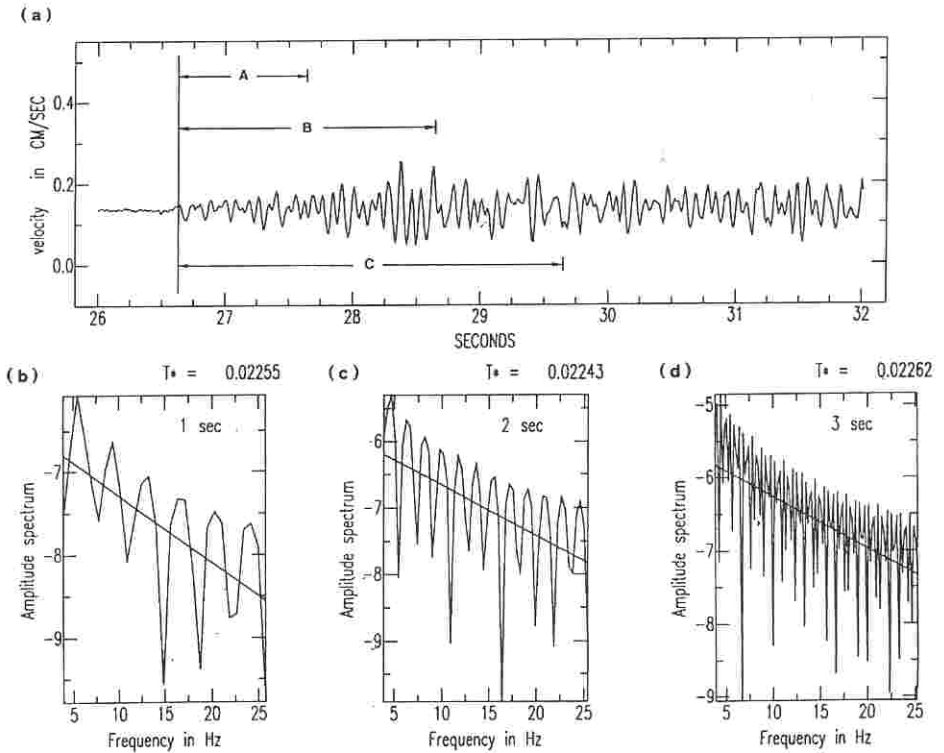
Figure 6. (a) Seismogram used for calculating the t* value and the three time
windows (denoted by A, B, and C); (b), (c) and (d) spectrum calculated from
the data truncated by window A, B and C. The regression line and the t*
value are also shown in each diagram.

    In this study, windowed seismograms were analyzed. The length of the time window wa
2 seconds. To examine whether the length of the time window would affect the value of th
calculated t_p*, different lengths (of time windows) were assigned for testing. The seismogra
used for the test is shown in Figure 6(a). Three time windows with lengths of 1, 2 and 3 sec a
shown in Figure 6(a) were assigned. The spectra and the fitting lines for determining the t*
these three cases are shown in Figures 6(b), 6(c) and 6(d). The values of t* were 0.0225
0.02243 and 0.02262 sec, respectively. These values show no significant difference, indicatin
that the length of the time window does not lead to large errors in the calculation of t*.
    Here the Fourier spectrum of the P- phases was obtained through the FFT method.
Parzen window taper was applied. Next the observed spectra were corrected for the source b
multiplying each spectra value by ω^2. Before looking at the spectra, the data were corrected fe
instrument responses to displacement, and then the slope of the spectrum with frequency rang
was determined by linear regression.
    To obtain the effects only caused by the weak zone of the Chinshan fault, the signals use
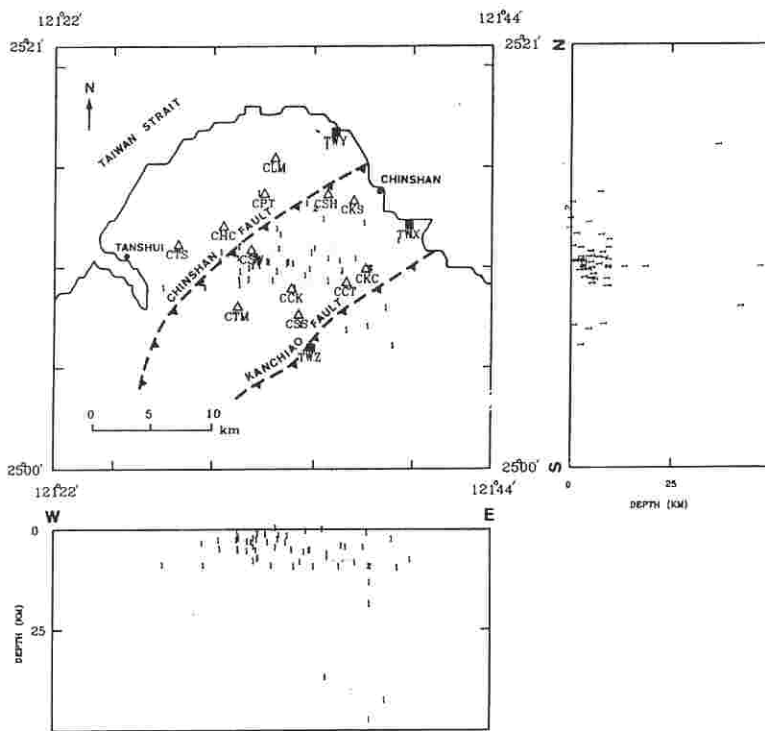had to have passed mainly through the zone. Fifty-seven events with epicentral distance ≤6

Figure 7. (a) Epicenters used to calculate the t* values; (b) depth distribution of events along the NS direction; (c) depth distribution of events along the EW direction. The numbers represent the magnitude of events.

km and focal depth ≤50 km were selected. Figure 7 shows the distribution of these events. The contours of the t_p* values are shown in Figure 8. The distribution pattern of the t* values is quite similar to that of the P-wave residuals. In this figure, a trend of relatively high t_p* values is revealed near the surface trace of the Chinshan fault. Although some relatively highs are also revealed in the Kanchiao fault area, their magnitude are somewhat lower, This means that the degree of attenuation of the Kanchiao fault is higher than that of Chinshan fault.
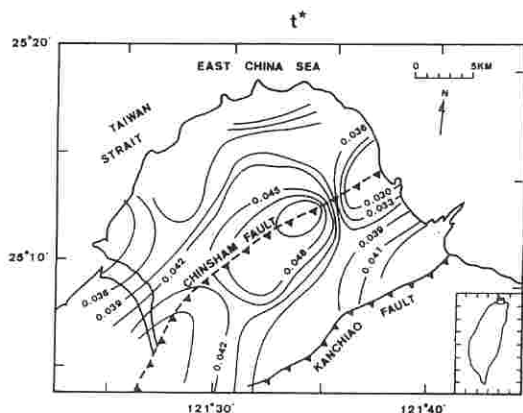

Figure 8. Contours of t_p* . The dashed lines denote the Chinshan fault and the Kanchiao fault. The contour lines with hachures denote the depression, and the hatches point toward the depression.

SEISMICITY AND FOCAL MECHANISMS

299 earthquakes in total were located by the temporary network and the three stations of the TTSN. Among them, 256 events were selected for analysis in this study. On the basis of the values of the root-mean-square error of the travel time residuals (RMS), the standard error of the epicenter (ERH) and the standard error of focal depth (ERZ) which were $\leq 0.3\ sec$, $\leq 2\ km$, and $\leq 2\ km$, respectively. Figure 9 shows the epicenters of the events. A also included are the two focal depth profiles along the NS and EW directions. Most of the earthquakes were located within the area bounded by the Chinshan fault and the Kanchiao fault. More than 95% of the events occurred at a depth shallower than 10 *km*, and mainly within the depth of from 0 to 5 *km*.

To find out the correlation between seismicity and the fault structure in this area, seven blocks (denoted by A to G) were separated along the strike of the Chinshan fault (see Figure 10). The focal depth profile corresponding to each section is also shown in Figure 10. A southeast-dipping seismic zone with an angle of about 55° can be delineated, which is similar to the dip angle of the Chinshan fault obtained from gravity data (Chen and Yeh, 1991). This might indicate that the seismic zone is related to the Chinshan fault.

Eighteen composite focal mechanisms were determined. Based on the first motions of the P-waves. Two orthogonal nodal planes, the fault and the auxiliary planes, which separate the first motions of the P-waves into compressional and dilatational quadrants on the focal sphere are shown in an/the equal-area projection of the lower hemisphere. The detailed technique of the determination is discussed elsewhere (e.g., Lee and Steward, 1981). Each mechanism was
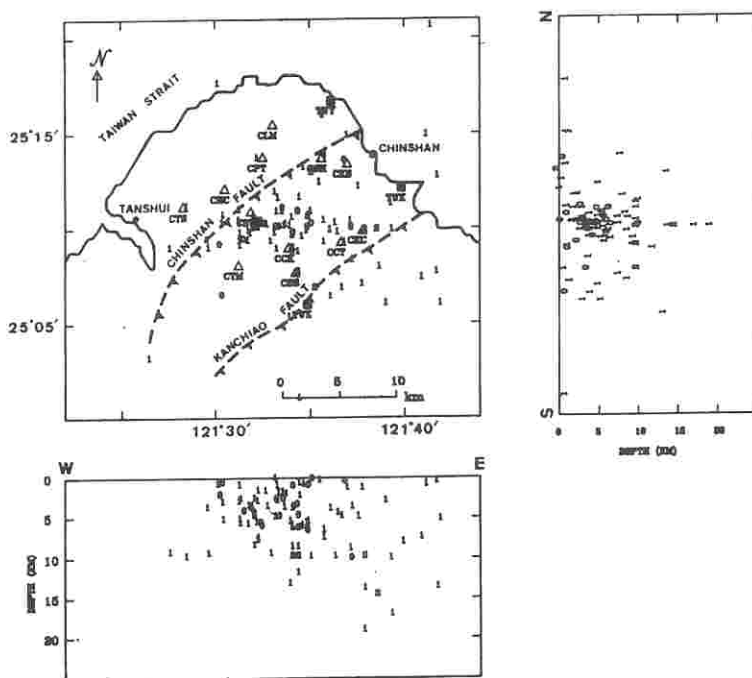

Figure 9. Epicenters located by the temporary network and focal depth profiles along the N-S and E-W directions. Seismographic stations are denoted by open triangles.
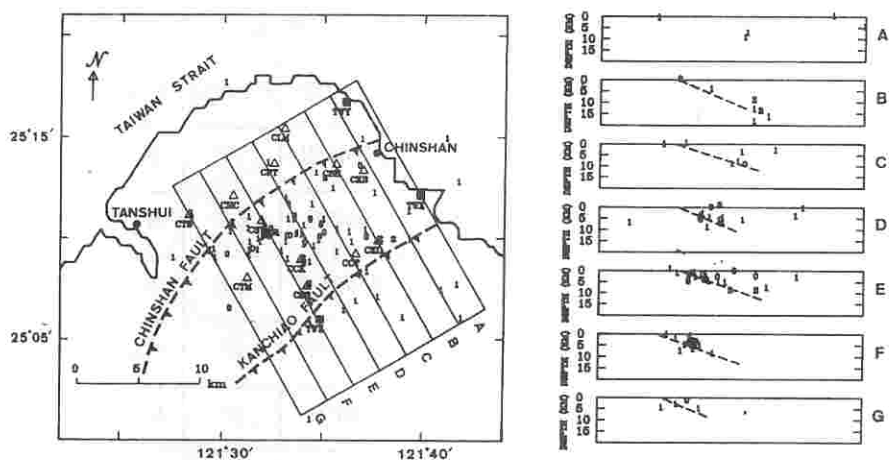
Figure 10. Depth profiles of events located by temporary network for blocks A-G. The dashed lines represent the fault in each block.
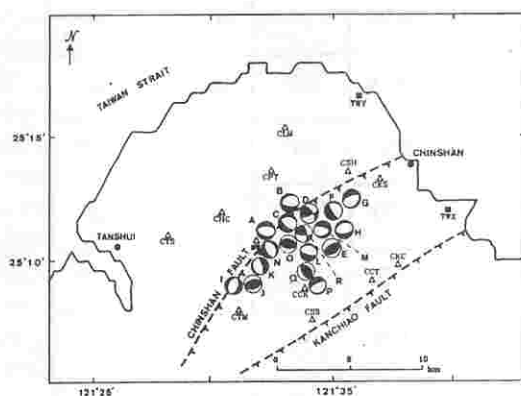

Figure 11. Equal-area projection of the lower hemisphere of the focal spheres. (The capital denoted in the top left corner represent the group names.)

obtained by combining the first motions of the P-waves from several earthquakes, under the assumption that these earthquakes have the same mechanism. Figure 11 shows the equal-area projection of the lower hemisphere of the composite focal sphere, and the parameters of these mechanisms are summarized in Table 3. Figure 12 shows the map view of the focal mechanisms. The black areas on each focal sphere indicate the quadrants of compressional first motions, while white areas indicate the quadrants of dilational first motions. Only four solutions are of the thrust type, whereas the other fourteen are of the normal type.

Table 3. Parameters of Focal Mechanism Solution of this study.

| Event	Plane 1		Plane 2		C-axis		T-axis	
	Strike	Dip	Strike	Dip	Azimuth	Plunge	Azimuth	Plunge
A	N55°W	40°SW	N77°W	52°NE	N140°E	77°	N22°E	6°
B	N78°W	64°SW	N62°E	32°NW	N48°E	66°	N178°E	16°
C	N52°W	46°NE	N52°W	44°SW	N142°W	89°	N38°E	1°
D	N53°E	72°SE	N47°W	60°NE	N179°W	8°	N84°W	35°
E	N55°E	54°NW	N55°E	36°SE	N36°W	9°	N144°E	81°
F	N47°W	80°SW	N71°E	20°NW	N62°E	52°	N152°W	32°
G	N26°E	30°SE	N59°E	64°NW	N180°	68°	N43°W	17°
H	N58°E	31°NW	N70°E	60°SE	N0°	73°	N155°E	16°
I	N16°E	40°NW	N16°E	50°SE	N86°W	85°	N106°E	5°
J	N74°E	50°NW	N74°E	40°SE	N15°W	5°	N165°E	85°
K	N12°W	20°NW	N12°W	70°NE	N104°W	65°	N78°E	25°
L	N69°W	20°NE	N69°W	70°SW	N22°E	65°	N158°W	25°
M	N65°E	35°SE	N66°W	65°NE	N114°W	62°	N 6°E	22°
N	N22°W	32°NE	N22°W	58°SW	N21°E	77°	N113°W	13°
O	N84°W	40°NE	N84°W	50°SW	N174°W	5°	N13°E	85°
P	N72°E	70°NW	N72°E	20°SE	N162°E	65°	N18°W	25°
Q	N14°W	50°SW	N30°W	40°NE	N112°W	5°	N124°E	81°
R	N86°W	70°SW	N 8°W	62°NE	N137°W	5°	N45°W	35°
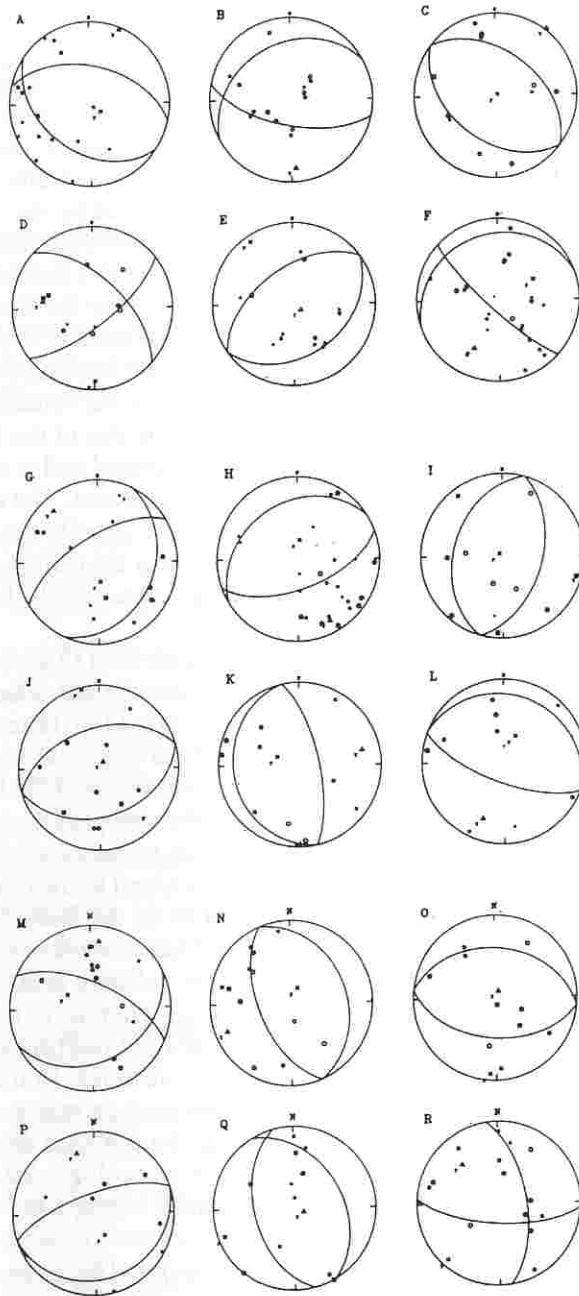
Figure 12. Map view of the focal mechanism (See Table 3 for the parameters. The area which the focal sphere covers is the approximate location area of the events with respect to each composite focal mechanism.)

DISCUSSION AND CONCLUSIONS

In general, the seismic wave velocity is controlled by the physical properties of the media, including the existing fissure, density, and temperature. The distribution of the P-wave travel time residuals (Figure 5) in this study reveals that one higher residual is underneath the Chinshan fault while another is underneath the Kanchiao fault. There two faults were also inferred by geologic data (Hsu, 1981). These higher residuals may be caused by the fracture zones of both faults and by the geothermal effect due to the Tatun and Chihsinshan volcanoes. Since most of the events used to calculate the P-wave travel time residuals were located in the southeast part of the study area, the seismic waves recorded at the stations near the Kanchiao fault could not pass through the volcanoes. The higher delay beneath the Kanchiao fault may only be caused by the fracture zone of this fault, whereas the higher residuals beneath the Chinshan fault may be caused not only by the fracture zone of the fault but also by the volcanoes. This is the reason that the delay in the area of the Chinshan fault is higher than that of the Kanchiao fault.

Anelasticity is an important property of the Earth's material and is strongly influenced by temperature, degree of partial melting and strength of the material. The relative high t_p^* value indicates a higher attenuation of seismic waves in the crust. Usually the fracture zone of fault exhibits higher attenuation. It is suggested that the highs near the Chinshan fault (Figure 7) are related to the fracture zone of this fault and to the volcanoes, whereas the high near the Kanchiao fault area may be related to the fracture zone of the fault.

The focal depth profiles perpendicular to the Chinshan fault (Figure 10) demonstrate that some earthquakes may be related to the fault and show that the dip of the fault is about 55° to the southeast. Results of the focal mechanisms indicate that 14 of 18 mechanisms are normal faulting. Ten of them strike in random directions whereas only four solutions(B,G,H and I) have a strike closely parallel to the Chinshan fault. The seismicities of the former, it is suggested, are uncorrelated to the Chinshan fault. If they were not, the strikes of these fault plane solutions would be confined in the same direction (or in a limited range of azimuth). In contrast, the seismicities of the latter are considered to possibly correspond to the Chinshan fault owing to the consistency of the strikes. These seismicities occur along the fault plane driven by gravity force. In other words, the movements in the Chinshan fault nowadays have become a normal type along the existing fault plane. Additionally, in most volcanic areas, as most seismicity is caused by gravity movements of a normal faulting type. Therefore, it is considered in this paper that the main cause of these seismicities with normal faulting are dominated by the geothermal activities of the Tatun and Chihsinshan Volcanoes. In the analysis here, four mechanisms are thrust faulting. The events of those four mechanisms were located at the fault plane of the Chinshan fault. The strikes and dips of the fault planes determined by the focal mechanisms are almost comparable to those inferred from geologic data (Hsu, 1981) and by gravity data (Chen & Yeh, 1991). It is believed that these earthquakes may be related to the activity of the Chinshan fault.

Data recorded by the temporary seismographic network and the three stations of the Taiwan Telemetered Seismographic Network in the Chinshan-Tanshui area were analyzed to determine the characteristics of the Chinshan fault. Seismicity, focal mechanisms, P-wave travel time residuals and t* have been/were included in the analyses. Both the distributions of the P-wave travel time residuals and the t_p^* values indicate that the Chinshan fault perhaps exists that location inferred from geologic data. This fault reveals low seismicity. His suggested that

most of the seismicity in this area corresponds to the activity of the volcanoes. The focal depth profile shows the dip of the fault is about 55° to the southeast. Based on the focal mechanism data, this fault is a thrust type. However, the activity of this fault may be normal or thrust, depending on the stress pattern in this area.

ACKNOWLEDGEMENTS

REFERENCES

Achauer, U., Greene, L., Evans, J.R. and Iyer, H.M. (1986) Nature of the magma chamber underlying the Mono Craters area, eastern California, as determined from teleseismic travel time residuals: *J. Geophys. Res.*, **91**, 13873-13891.

Bakun, W.H. and Bufe, C.G. (1975) Shear wave attenuation along the San Andreas fault zone in central California: *Bull. Seism. Soc. Am.*, **65**, 439-459.

Bakun, W.H., Bufe, C.G. and Stewart, R.M. (1976) Body wave spectra of central California earthquakes: *Bull. Seism. Soc. Am.*, **66**, 439-459.

Barker, T. and Stevens, J.L. (1983) Shallow shear wave velocity and Q structures at the El Centro strong motion accelerography array: *Geophys. Res. Lett.*, **10**, 853-856.

Ben-Menahem, A., Rosenman, M. and Israel, M. (1972) Source mechanism of the Alaskan earthquakes of 1964 from amplitude of free oscillations and surface waves: *Phys. Earth Plant. Inter.*, **5**, 1-29.

Brune, J.N. (1970) Tectonic stress and the spectra of seismic shear waves from earthquakes: *J. Geophys. Res.*, **75**, 4997-5009.

Chang, Stanley, S.L. (1968) Regional stratigraphic study of the Lower Miocene Formations in northern Taiwan: *Petrol. Geol. Taiwan*, **6**, 47-70.

Chen, K.J. and Yeh, Y.H. (1991) Gravity and microearthquake studies in the Chinshan-Tanshui area, northern Taiwan: *Terrestrial, Atmospheric and Oceanic Sci.*, **2**, 35-50.

Chou, J.T. (1962) Stratigraphic and sedimentary study of the Mushan Formation in northern Taiwan: *Petrol. Geol. Taiwan, Mr. King's Jubilee*, **1**, 87-119.

Gladwin, M.T. and Stacey, F.D. (1974) Anelastic degradation of acoustic pulses in rock: *Phys. Earth Plant. Inter.*, **8**, 332-336.

Ho, C.S. (1974) The Taipei fault and related structural features in northern Taiwan: *Proc. Geol. Soc. China*, **17**, 95-109.

Hsu, M.Y. (1967) Geology of the coal field between Chinshan and Shihmen, northern Taiwan: *Bull. Geol. Surv. Taiwan*, **19**, 15-26 (in Chinese), 9-14. (in English).

Hsu, T.L. (1981) Geological map of Taiwan, Linkou sheet, Sanchih sheet, and Taipei sheet, Geol. Surv. ROC.

Kanamori, H. (1967) Spectrum of short-period core phases in relation to the attenuation in the mantle: *J. Geophys. Res.*, **72**, 2181-2186.

Kanamori, H. and Anderson, D.L. (1977) Importance of physical dispersion in surface wave and free oscillation problems: Review: *Rev. Geophys. Space Phys.*, **15**, 105-112.

Knopoff, L.Q. (1964:) *Rev. Geophys.*, **2**, 625-660.

Lee, W.H.K. and Lahr, L.C. (1972) HYPO71: *A computer program for determining hypocenter, magnitude, and first motion pattern of local earthquakes*: USGS Open File Rept., 100 pp.

Lee, W.H.K. and Steward, S.W. (1981) *Principles and Applications of Microearthquake Networks*: Academic Press, London, 293 pp.

Lee, W.H.K., Bennett, R.E. and Meagher, K.L. (1972) *A method of estimating the magnitude of local earthquakes from signal duration*: U. S. Geol. Surv. Open File Rep., 100pp.

Reiter, L. and Monfort, M. E. (1977) Variations in initial pulse width as a function of anealastic properties and surface geology in central California: *Bull. Seism. Soc. Am.*, **67**, 1319-1338.

Solomon, S.C. (1972) Seismic wave attenuation and partial melting in the upper mantle of North America: *J. Geophys. Res.*, 77, 1483-1502.

Solomon, S.C. (1973) Shear wave attenuation and melting beneath the mid-Atlantic ridge: *J. Geophys. Res.*, **78**, 6044-6059.

Teng, T.L. (1968) Attenuation of body waves and the Q structure of the mantle: *J. Geophys. Res.*, **73**, 2195-2208.

Yeh, Y.H. and Tsai, Y.B. (1981) Crustal structure of central Taiwan from inversion of P-wave arrival times: *Bull. Inst. Earth Sci. Acad. Sin.*, **1**, 83-103.

金山斷層之地震學研究

陳光榮[1]、葉義雄[2]、顏宏元[2]、林正洪[2]

1. 國立臺灣師範大學地球科學研究所
2. 中央研究院地球科學研究所

摘 要

本研究於 1989 年利用微震調查方法，在金山淡水地區設置由十二個測站（三分量數位式）組成之臨時測震網，以期瞭解金山斷層之地震活動特性。本文分析由該測震網與中央研究院地球科學研究所台灣區遙記式測震網的部份測站所蒐集之資料。其結果顯示 P 波走時剩餘及 t_p^* 的分佈指出該斷層存在的位置，大約與由地質資料所判定的位置相同。由地震的時空分佈顯示該斷層的地震活動並不頻繁。這些地震集中於一傾角大約為 55° SE 之斷層面上。由震源機制說明金山斷層雖為逆斷層型態，但其活動有時為逆斷層，有時為正斷層，視本地區的應力型態而定。

關鍵詞：P 波走時、t_p^* 值